

# The Inverse-Square Law Force between Vapor-Mediated Droplets

Zhi Wu Jiang<sup>1</sup>, Hang Ding<sup>1</sup>, and Er Qiang Li<sup>1\*</sup>

<sup>1</sup>*Department of Modern Mechanics, University of Science and Technology of China, Hefei 230027, China*

(Dated: This manuscript was compiled on October 7, 2021)

In 1687, Sir Issac Newton published *The Mathematical Principles of Natural Philosophy* [1] in which the law of universal gravitation was derived. It is the first inverse-square law discovered in nature, combined with Coulomb's law in 1785 [2], the two famous inverse-square laws become part of the foundation of physics. Why does nature prefer inverse-square laws over the laws of other forms? The question is still arousing broad discussion, and it is an important topic in physics. So far, the origin of inverse-square law is still under exploration although from the point of reductionism, the law of universal gravitation can be treated as the approximation of Einstein's general relativity under weak gravitation [3], and Coulomb's law could be derived from quantum electrodynamics [4]. Here we discover a new inverse-square law between evaporating droplets deposited on a high energy solid substrate. For binary droplets, we show that the evaporation from a source droplet will create a surface tension gradient in the precursor film of a target droplet, resulting in a long-range inverse-square law force acting on the target droplet, and that the inverse proportion decay of the source vapor concentration in the space essentially contributes to the inverse-square form of the force. Furthermore, the inverse-square law force here is shown to hold for all experimental parameters tested, and other systems such as pure-liquid-droplet system and thermocapillary system, and it satisfies the superposition principle, not only suggesting exciting directions for future droplet research and applications, but also benefiting understanding of nature's predilection for inverse-square law.

The inverse-square law states that a physical quantity is inversely proportional to the square of the distance  $r$ , from the source of that physical quantity. Its concise expression greatly advances our understanding of fundamental physical principles. In fluid mechanics field, an analogue of the Newton law of gravity or Coulomb's law was first proposed to describe the lateral capillary interaction between particles bound to interfaces [6]. Such an interaction force generally originates from the overlap of perturbations at interfaces, which may be attributed to gravity of floating particles (also known as the Cheerios effect [7]), wetting of particles [8], or elastic deformation of soft substrates by droplets (the inverted Cheerios effect [9]). Paunov *et al.* [6] showed that the lateral capillary force obeyed a power law resembling the two-dimensional Coulomb's law in certain range of interparticle distances, and defined the so-called capillary charge to mimic electric charges.

This analogue makes us wonder what will happen between two evaporating sessile droplets, as their evaporating fields overlap like the above mentioned perturbations at interfaces do. Evaporating sessile droplets abound in nature and technology, forming an important ramification of two-phase flows [10]. Understanding their behavior can be rewarding for advancing interfacial mechanics [11, 12] and industrial applications [13–15]. For droplets consisting of miscible liquids, they attract if the more volatile component has higher surface tension [16]. As shown in Fig. 1a (a copy sketch to fig. 3a from Cira, Benusiglio & Prakash [5]), higher vapor concentration

between the droplets leads to less evaporation of at proximal sides (e.g. right-side for the left droplet) than distal sides of the two droplets. Consequently, more volatile component liquid with higher surface tension will persist at proximal sides, creating a net surface tension force pulling two droplets toward each other. Such a movement triggered by surface tension gradients is also referred to as Marangoni effect [17]. For droplets made of pure liquids, they could also move, as similar droplet arrangement in Fig. 1a will also cause nonuniform vapor density [18, 19], which in turn leads to subsequent variations of the evaporation-induced contact angles or the thermocapillarity effect [16]. Nevertheless, compositional surface tension gradients are usually orders of magnitude larger than the thermal ones [20, 21].

In the above studies, different integral forms rather than analytical solutions were used to calculate the net surface tension force or the driving force [5, 22], which qualitatively matched with experimental data. In this study, we show for the first time that the interaction force between two evaporating sessile droplets is an inverse-square law force and validate our theory with high precision experimental data.

In our experiments, two droplets made of the same propylene glycol (PG) aqueous solution were produced from a minuscule capillary tube and were dropped onto a pristine oxygen plasma cleaned silicon wafer, and the interaction between them was acquired with a high resolution digital camera (8K RED DSMC2 Camera, RED Digital Cinema, LLC.). To control the surroundings humidity and temperature, droplet experiments were carried in an environmental chamber (5503-1-11-100-1741 Mini Glove Chamber, Electro-Tech Systems, Inc.) which provided transparent walls for good visibility. A sketch

\* eqli@ustc.edu.cn

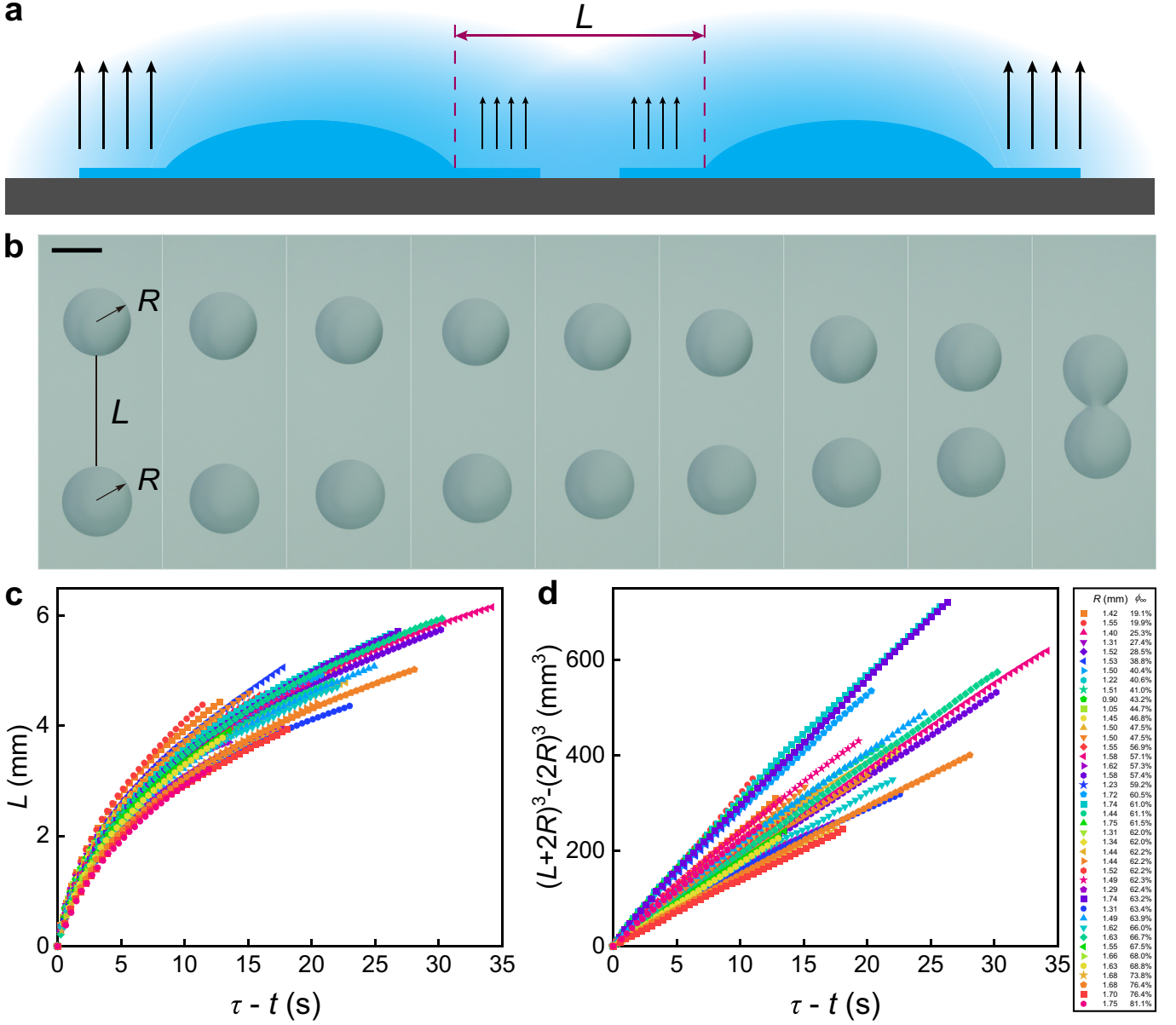


FIG. 1. Attraction between two binary droplets. (a) A copy sketch to fig. 3a in [5] showing the vapor gradients (blue shading) and evaporation (upward arrows) from two sessile binary droplets. (b) Top view showing attraction of two 10 wt% PG sessile droplets of the same size on a hydrophilic silicon substrate. The spreading radius of droplets is  $R = 1.37$  mm, ambient relative humidity  $\phi_\infty$  is 51.3%, room temperature is 20°C, the time of droplet contact is  $\tau = 22$  s. Sequence of images spaced by 2.75 s. Scale bar is 2 mm. (c) Evolution of the distance  $L$  between two droplets with time  $\tau - t$  for various  $R$  and  $\phi_\infty$ . (d) All data in (c) fall into straight lines implying a linear relationship of  $(L + 2R)^3 - (2R)^3 \sim \tau - t$ . Values of  $R$  and  $\phi_\infty$  are listed in the legend.

of experimental setup and properties of liquids used in the study can be found in Supplementary Information section I. Parameter tested ranges from 0.07 - 0.80  $\mu\text{L}$ , 19.9% - 81.1%, for droplet volume  $\Omega$  and relative humidity (RH)  $\phi_\infty$  in the environmental chamber, respectively. When a droplet consisting of miscible liquids is located on a superhydrophilic substrate, it has shown that the interplay among Marangoni flow, capillary flow, diffusive transport, and evaporation will lead to a droplet profile with an apparent nonzero contact angle, even though

each of the liquid components fully wets the substrate [5, 12, 21]. This phenomenon is also observed in our experiments for 10 wt% PG droplets (Fig. 2c). Repeatability test (Supplementary Information Fig. S1) shows good reliability of experimental measures. Figure 1b shows the attraction and later coalescence of two 10 wt% PG droplets with a distance  $L$  apart, the mean spreading radius  $R = 1.37$  mm and environmental relative humidity  $\phi_\infty = 51.3$  %. Figure 1c shows the change of  $L$  verse time  $\tau - t$ , for various trials with  $R \in [0.8, 1.8]$  mm and

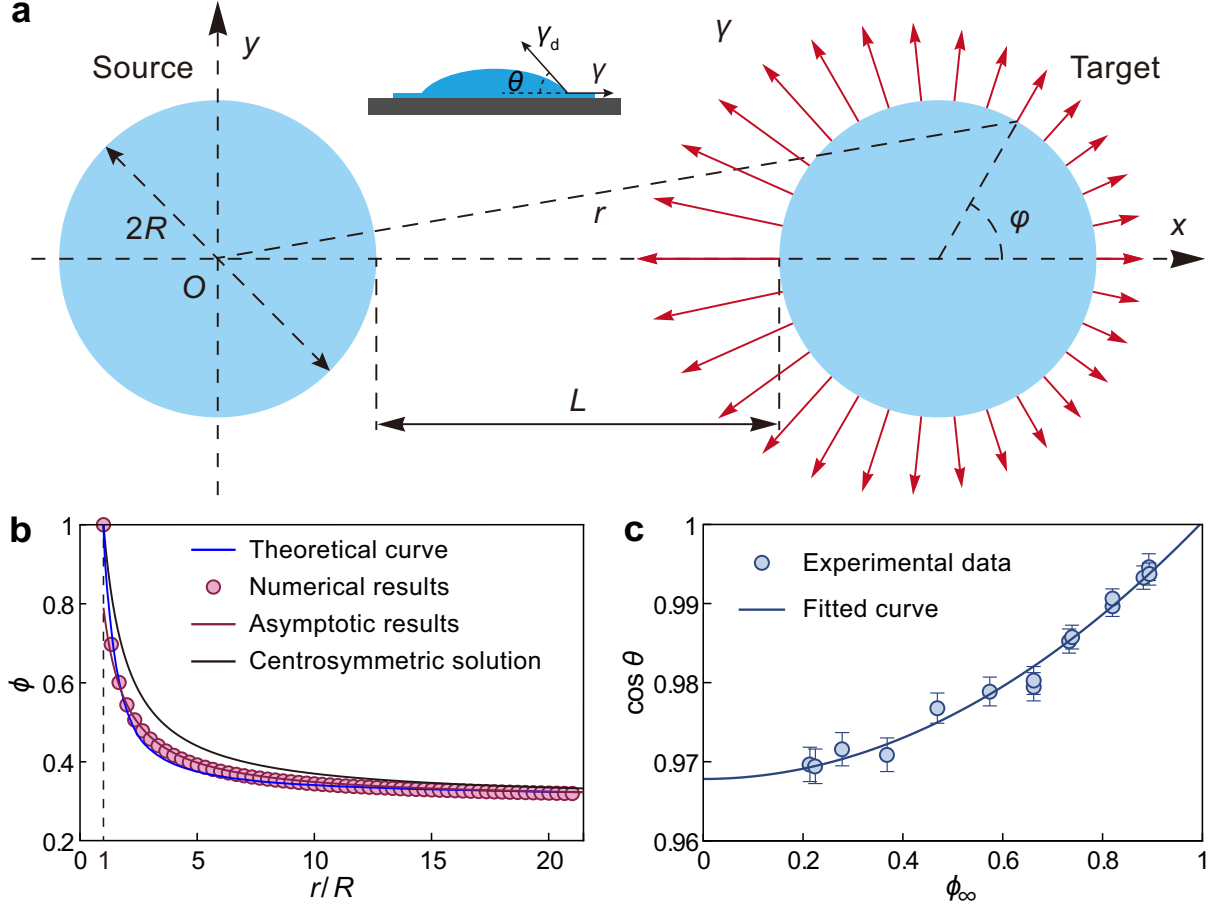


FIG. 2. Dependence of contact angle on evaporation from a “Source” droplet. (a) Schematic showing the change in surface tension  $\gamma$  along the periphery of the “target” droplet, as a result of evaporation from the “source” droplet. The inset:  $\gamma_d$  the surface tension of the bulk droplet liquid,  $\gamma$  the surface tension in the precursor liquid film, and  $\theta$  the contact angle, respectively. (b) The local relative humidity  $\phi$  along the solid substrate.  $r/R$  is the dimensionless distance. Blue curve: theoretical results of  $\phi$  (Eq. S10 in Supplementary Information), for the evaporation of a thin film with  $\theta = 0$ . Dots: numerically solved results of  $\phi$  for the evaporation from a sessile droplet. Parameters used in the simulation: the ambient humidity in the far field  $\phi_\infty = 30.0\%$ ,  $\theta = 10^\circ$ . Red curve:  $\phi(r) = \lambda(1 - \phi_\infty)R/r + \phi_\infty$ , an asymptotic solution of Eq. S10 with  $\lambda = 0.7$ . Black curve: centrosymmetric solution of  $\phi(r)$  for the evaporation from a droplet floating freely in the air. Liquid is 10 wt% PG aqueous solution. (c) Contact angle as a function of  $\phi_\infty$  for a 10 wt% PG droplet on a hydrophilic silicon surface.

$\phi_\infty \in [19.9\%, 81.1\%]$ , where  $\tau$  is the moment of first contact of two droplets. Previously experimental data was also presented in such a way [5], which we believe is not conducive to further mechanism exploration. Instead, after a transformation, Fig. 1d shows a very interesting result that all curves transform into straight lines through the origin. Despite of the seemingly meaningless arrangement of  $(L + 2R)^3 - (2R)^3$ , in the following we will show the concise and crucial physics implied by

$$(L + 2R)^3 - (2R)^3 = k(\tau - t). \quad (1)$$

The differential form of Eq. 1 reads  $-3dL/dt = k/(L + 2R)^2$ , or

$$-6U = k/(L + 2R)^2 \quad (2)$$

with the kinematic relationship of  $2U = dL/dt$ , where  $U$  is the velocity of the moving droplet. For a Stokes flow

considering here [5], the drag force  $F_d = 3\pi\mu R U l_n / \theta \propto U$  during droplet motion is mainly originated from the region near the contact line [5, 23], and is balanced by the driving force  $F$ . Here  $\mu$  denotes the dynamic viscosity of the liquid,  $\theta$  is the contact angle,  $l_n$  is the logarithmic cut-off coefficient [11]. Consequently, the right-hand term in Eq. 2 can be comprehended as the driving force with an inverse square law form, as  $L + 2R$  clearly represents the distance between centers of two droplets!

The deduction here is quite similar to the method used by Sir Issac Newton when he derived the law of universal gravitation from Kepler’s three laws and the Newton’s law of motion proposed by himself. Nevertheless, the law of universal gravitation is derived from pre-existing indisputably laws, here the origin of the inference e.g. Eq. 1, is just a new empirical formula. Therefore, in the following we will thoroughly discuss the new inverse-square

force from various aspects, including its “propagator”, precise form, and universal applicability.

The origin of the driving force  $F$  has been revealed [5] and described above. Here we propose that evaporated vapour molecules could be comprehended as “propagator” for vapor-induced driving forces. For PG-water mixture, vapor pressure of PG is negligible at room temperature and vapor mainly originates from water evaporation. Therefore, the local vapor concentration can be replaced by relative humidity  $\phi(r)$ , or  $\phi$  for simplicity, where  $r$  denotes the distance from center of the “source” droplet (Fig. 2a). It is shown that  $\phi$  satisfies the Laplace equation [24],  $\nabla^2\phi = 0$ , which has a centrosymmetric solution of  $\phi(r) = (1 - \phi_\infty)R/r + \phi_\infty$  (black curve in Fig. 2b), for a droplet floating freely in the air, where  $\phi_\infty$  denotes the ambient humidity far from droplets. Here for a spherical segment droplet with a finite contact angle  $\theta$ , the Laplace equation was solved numerically with finite element method software FreeFem++. Despite of the fact that  $\phi$  also changes with  $\theta$ , it converges to a single curve when  $\theta \leq 30^\circ$  (Fig. S3). Meanwhile, for a liquid film with  $\theta = 0^\circ$ , we are able to derive an analytic solution of  $\phi$  (blue curve in Fig. 2b, see detailed derivation in Supplementary Information section II). Therefore, we can use Eq. S10 to determine  $\phi$  for droplets with a contact angle  $\theta \leq 30^\circ$ . For simplicity,  $\phi(r) = \lambda(1 - \phi_\infty)R/r + \phi_\infty$ , an asymptotic solution to Eq. S10 with  $\lambda = 0.7$ , will be used in later analysis where  $\theta \in [5^\circ, 15^\circ]$ . The distribution of  $\phi(r)$  produces a gradient in  $\gamma$ , the surface tension of the precursor liquid, and subsequently the driving force for droplet motion [5]. Figure 2a schematically shows the change in  $\gamma$  along the periphery of “target” droplet.

To calculate the force  $F$ , the dependence of  $\gamma$  on  $\phi(r)$  needs to be pinned down. This can be challenging for direct measurement. In practice we choose to measure the change of contact angle  $\theta$  with  $\phi_\infty$  as  $\gamma$  is directly connected with  $\theta$  by  $\gamma = \gamma_d \cos \theta$ , where  $\gamma_d$  represents the surface tension of the bulk droplet liquid (inset figure in Fig. 2a). The best fit to our experimental data in Fig. 2c provides an empirical formula  $\cos \theta = f(\phi) = m_p \phi^2/2 + b_p$ , with fitting parameters  $m_p = 0.065$  and  $b_p = 0.97$ . Different power-laws have also been proposed [5, 21], nevertheless, we believe the choice of exponents may affect the concrete form of  $F$ , but will not change its inverse-square nature which is strongly implied by Eq. 1.

Now it is time to calculate  $F$ . The surface tension gradient  $\Gamma$  reads

$$\Gamma = \frac{d\gamma}{dr} = \frac{d\gamma}{d\phi} \frac{d\phi}{dr} = -\gamma_d m_p \phi_\infty \frac{\lambda(1 - \phi_\infty)R}{r^2}. \quad (3)$$

For droplets apart far away from each other ( $r \gg R$ ), assuming  $\Gamma$  is a constant and taking the value at center of “target” droplet, with Gauss’s flux theorem, we get the force along  $x$ -axis

$$F = \pi R^2 \Gamma = -\frac{\gamma_d m_p \phi_\infty \lambda \pi R^3 (1 - \phi_\infty)}{(L + 2R)^2}. \quad (4)$$

It is an inverse-square force! Besides above approximate

calculation, a rigid derivation of  $F$  can be found in Supplementary Information section IV, in which the exact same form of  $F$  is obtained with third order accuracy.

To verify Eq. 4, a direct way is to compare  $F$  with the drag force  $F_d = 3\pi\mu R U l_n/\theta$ . Before that, we first investigate the veracity of  $F_d$  and pin down its cut-off coefficient  $l_n$ . Herein droplets were released onto and slid down along a clean silicon wafer tilted  $15^\circ$  from horizontal line. Droplet volume  $\Omega$  was measured by a Phantom v2512 CMOS high-speed video camera from side view. Droplet slide motion along silicon wafer was acquired with a RED DSMC2 Camera perpendicular to substrate, to determine droplet terminal velocity  $U_t$  (Fig. S6 in Supplementary Information). The gravity force component along wafer  $F_g = \rho\Omega g \sin 15^\circ$ , where  $g$  is the gravity acceleration, should be balanced with the drag  $F_d = 3\pi\mu R U_t l_n/\theta$  once droplet reaches its terminal velocity. Figure 3a shows an excellent agreement between calculated  $F_g$  and  $F_d$  (dots in red). Cut-off coefficient  $l_n$  is determined to be 17.8, close to 15 reported for liquid spreading on dry surfaces [25]. Figure 3a also draws drag force calculated from  $F_d \sim \gamma R C a^{2/3}$  (dots in blue), another widely used model based on the Cox-Voinov theory which considers apparent contact angle change during motion [11, 26–28] (see more details in Supplementary Information section V). It is shown that  $3\pi\mu R U_t l_n/\theta$  agrees better with experimental data, implying amendment may be needed for applying the Cox-Voinov theory to scenarios where Marangoni contraction is involved in [21, 29]. Giving the model of the drag force, the influence of droplet deformation on droplet motion as  $\tau - t$  approaches zero is investigated and found to be negligible (Fig. S7 and Supplementary Information section VI).

Back to the previous problem, now we can verify Eq. 4 with kinematic data shown in Fig. 1. Balancing drag force  $F_d = 3\pi\mu R U l_n/\theta$  with driving force  $F$  in Eq. 4, we get  $U = -\gamma_d m_p \lambda R^2 \theta \phi_\infty (1 - \phi_\infty) / [3\mu l_n (L + 2R)^2]$ . Combining with Eq. 2, the prefactor in Eq. 1 finally reads

$$k = 2\gamma_d m_p \lambda R^2 \theta \phi_\infty (1 - \phi_\infty) / \mu l_n. \quad (5)$$

Red dots in Fig. 3b show a good agreement between the prefactors  $k_t$  calculated from Eq. 5, and  $k_e$  measured experimentally from Fig. 1d, for  $\phi_\infty \sim 60\%$ . If we take a linear model of  $\cos \theta = m_l \phi + b_l$  [5], or  $\theta = m_t (\phi_{eq} - \phi)^{1/3}$  [21], the calculated prefactors  $k_t$  marked by gray and blue dots respectively in Fig. 3b remain consistent with  $k_e$ . For harsher experimental conditions with  $\phi_\infty < 25\%$  or  $> 75\%$ ,  $k_e/k_t$  calculated from all three models deviate from 1, but still spread mainly between 0.5 and 1.5 (Fig. 3c). The deviation possibly originates from the use of  $\theta = f(\phi_\infty)$  to predict the influence of local relative humidity on  $\theta$  (Fig. 2c). A more precise model of  $\theta = f(\phi)$  may worth pursuing, nevertheless, Fig. 1d has demonstrated that Eq. 1 holds for all tested experimental conditions with  $\phi_\infty \in [19.1\%, 81.1\%]$ , indicating the inverse-square nature of  $F$  is beyond reasonable doubt.

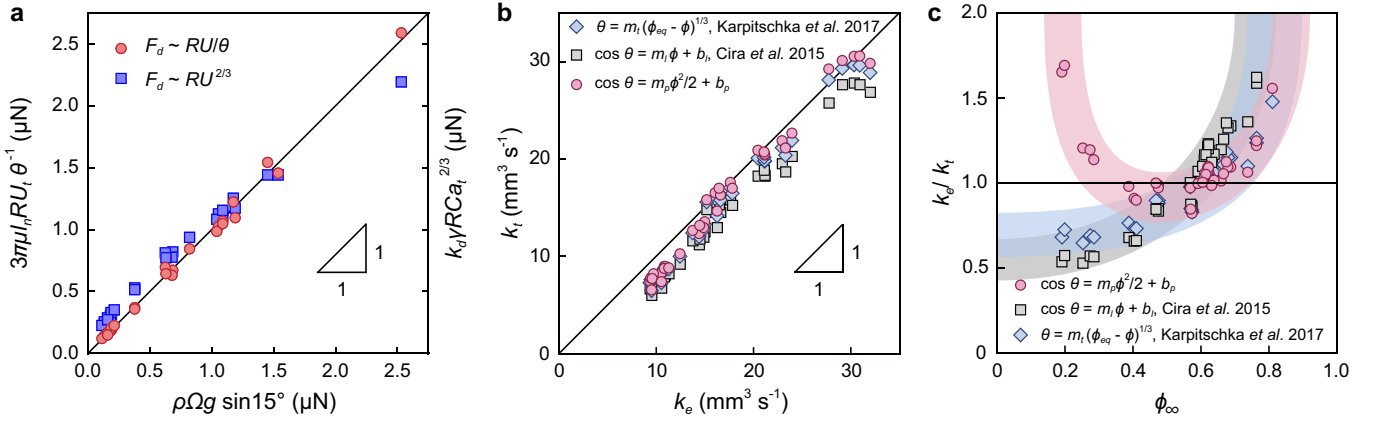


FIG. 3. Investigation on two models of drag force and three models of  $\theta = f(\phi)$ . (a) Comparison between drag force and gravity force component along the substrate. The straight line has a slope of 1. (b) Comparison between the prefactors  $k_t$  calculated theoretically from Eq. 5, and  $k_e$  measured experimentally from Fig. 1d, for the three different models of contact angle. Data are selected for  $\phi_\infty \sim 60\%$ . (c) The ratio of  $k_e/k_t$  versus environment humidity  $\phi_\infty \in [19.9\%, 81.1\%]$ . Fitting coefficients are  $m_p = 0.065$  and  $b_p = 0.97$ ,  $m_l = 0.036$  and  $b_l = 0.96$ ,  $m_t = 0.28$  and  $\phi_{eq} = 0.95$ , for the three different models of contact angle, respectively.

Next we investigate the universal applicability of the inverse-square law force  $F$ . The first test is for two droplets of unequal size. Our experimental results (Fig. 4a, also see Figs. S9-10 in Supplementary Information) show that the kinematic relationship satisfies

$$(L + R_1 + R_2)^3 - (R_1 + R_2)^3 = k'(\tau - t), \quad (6)$$

where  $R_1$ ,  $R_2$  denotes the spreading radius of the two droplets, respectively. Equation 6 has essentially the same form as Eq. 1, implying the inverse-square nature of the force. Previously, we have shown the feasibility of using the value of  $\Gamma$  at center of “target” droplet to calculate  $F$ . Similarly, resultant force on “target” droplet here reads  $F_{12} = \pi R_2^2 \Gamma = -\lambda m_p \gamma_d \phi_\infty \pi R_1 R_2^2 (1 - \phi_\infty) / (L + R_1 + R_2)^2$ , if we take the previously used empirical model  $\cos \theta = m_p \phi^2 / 2 + b_p$ . Meanwhile, the “target” droplet will exert a force on the “source” droplet reads  $F_{21} = \pi R_1^2 \Gamma = -\lambda m_p \gamma_d \phi_\infty \pi R_2 R_1^2 (1 - \phi_\infty) / (L + R_1 + R_2)^2$ . It is evident that for different sized droplets,  $F_{12} \neq F_{21}$ , indicating they are not action and reaction forces. A complete derivation of the force here with accuracy analysis can be found in Supplementary Information section VII. For  $0.37 < R_1/R_2 < 2.70$ , the error to above  $F_{12}$  and  $F_{21}$  will be less than 20%. Meanwhile, the calculated  $k_e/k_t$  is nearly equal to 1 for moderate droplet size ratio but increases to 1.7 for very unequal droplet sizes (Fig. 4a). Anyhow, Eq. 6 indicates with great certainty the inverse-square nature of the force, which is profoundly important than the concrete form of it.

Figure 4b implies that the inverse-square form of  $F$  holds when concentration of PG water solution changes. After being redrawn, data extracted from previous studies of two pure *n*-Hexane droplets on a solid substrate (Fig. 4c) [16], and of floating binary droplets on a liquid free surface (Fig. 4d) [30], indicate that the inverse-square force also applies to such pure-liquid-droplet sys-

tem and thermocapillary system. For the latter, nonuniform vapor density produces a temperature gradient over the cap of the floating droplet and subsequently a thermocapillary stress contributing to droplet motion [30]. The linear dependence of thermal stress on temperature, combining with the inversely proportional decay of temperature in the space, guarantees the inverse-square form of the force, evidenced by  $(L_0 + 2R)^3 - (L + 2R)^3 \propto t$ , where  $L_0$  is the initial edge-to-edge distance between droplets (see detailed derivation in Supplementary Information section VIII). To obtain a straight line through the origin, time  $t$  rather than  $\tau - t$  in Fig. 4d is used to present the kinematic relationship. The reason lies in that the thermally affected zones of two droplets will overlap as distance  $L$  keep decreasing, which in turn interferes droplet motion, evidenced by data deviation from prediction for  $t > 50$  s.

Next, the key factors in the evaporation-induced inverse-square force will be discussed from a perspective analogous to the law of universal gravitation. For gravitational force, when a target object with mass  $m$  perceives the inverse proportion decay gravitational potential of a source object  $E = -GM/r$ , it will be attracted by the inverse-square force  $F_m = GMm/r^2$ , where  $G$  is the gravitational constant and  $M$  is the mass of source object. Analogically, we define a humidity potential  $E' = -G'M'/r = -\gamma_d m_p \phi_\infty \lambda (1 - \phi_\infty) R_1 / r$  which also decays inversely proportional to distance, where  $G' = d\gamma/d\phi = \gamma_d m_p \phi_\infty$  is a constant denoting the derivative of surface tension to environment humidity,  $M' = \lambda(1 - \phi_\infty)R_1$  represents the decay coefficient of humidity away from the source droplet,  $m' = \pi R_2^2$  represents the wetting area of the target droplet and  $r$  denotes the distance between the centers of the two droplets, respectively. In an identical coordinate system as the universal gravitation (Fig. 5), when a target droplet senses

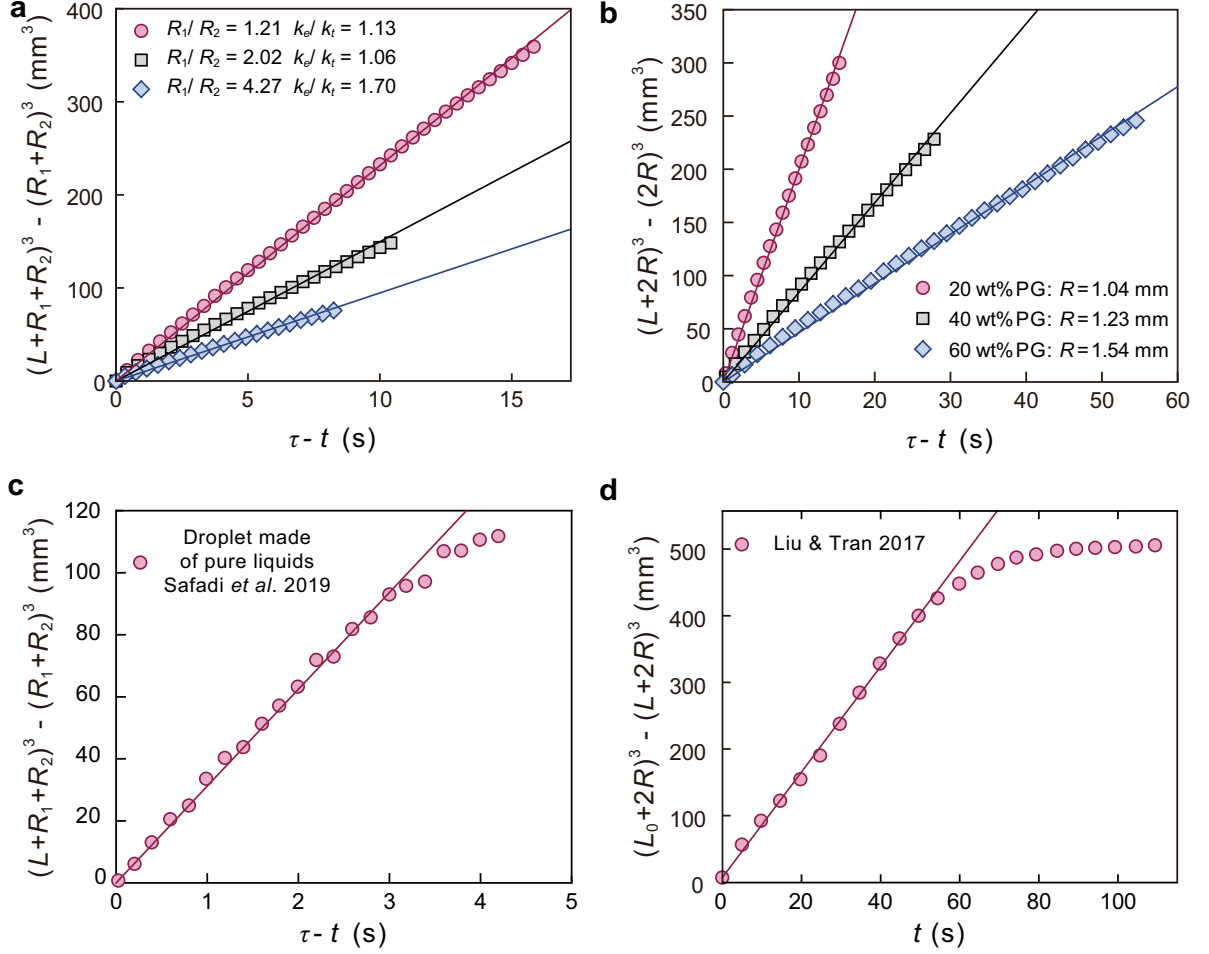


FIG. 4. Universal applicability of the inverse-square law force between vapor-mediated droplets. Data fall into straight lines implying an inverse-square force between (a) 10 wt% PG droplets of different sizes, (b) PG aqueous droplets of different concentrations, and (c) droplets made of pure liquid (experimental data extracted from Sadafi *et al.* [16]). (d) Attraction of two 80 wt% IPA aqueous droplets floating on a silicone oil pool. Data in early stage fall into a straight line, implying an inverse-square force. Deviation occurs when thermally affected zones of two droplets overlap, which brings other force into play and interferes droplet motion. Data are extracted from Liu & Tran [30].

$E'$ , it will be attracted by a force

$$F = \frac{\gamma_d m_p \phi_\infty \lambda \pi R_1 R_2^2 (1 - \phi_\infty)}{(L + R_1 + R_2)^2} = G' \frac{M' m'}{r^2}. \quad (7)$$

It is worth noting that compared with previous force expression,  $F$  in Eq. 7 lacks a negative sign, as positive directions of force in the two coordinates in Fig. 2a and Fig. 5 are opposite.

In nature, an important manifestation of the law of universal gravitation and Coulomb's law is the satisfaction of the superposition principle. The superposition of the humidity field is not that straightforward as there is an upper limit for humidity, which is 1. A detailed description of calculation and fitting of the total humidity distribution from two "source" droplets can be found in Supplementary Information section IX. For simplicity, considering two droplets of the same spreading radius  $R$ , their total humidity is expressed as  $\phi =$

$\lambda'(1 - \phi_\infty)R/r_1 + \lambda'(1 - \phi_\infty)R/r_2 + \phi_\infty$ , where  $\lambda'$  is a fitting parameter dependent on the distance between two droplets (Fig. S12),  $r_1$  and  $r_2$  are distances between "target" and the two "source" droplets (Fig. 5). Not surprisingly, the humidity from multiple droplets satisfies the superposition principle. For an ideal small "target" droplet which does not affect  $\phi$ , the resultant force exerting on it reads

$$\vec{F} = G' \frac{M' m'}{r_1^2} \vec{n}_1 + G' \frac{M' m'}{r_2^2} \vec{n}_2, \quad (8)$$

where  $G' = \gamma_d m_p \phi_\infty$ ,  $M' = \lambda'(1 - \phi_\infty)R$ ,  $m' = \pi a^2$ ,  $a$  is the radius of the ideal small "target" droplet,  $\vec{n}_1$  and  $\vec{n}_2$  are the unit vectors pointing from center of "target" to the center of two "source" droplets, respectively. The resultant force has an equivalent form as the superimposed gravitational force.



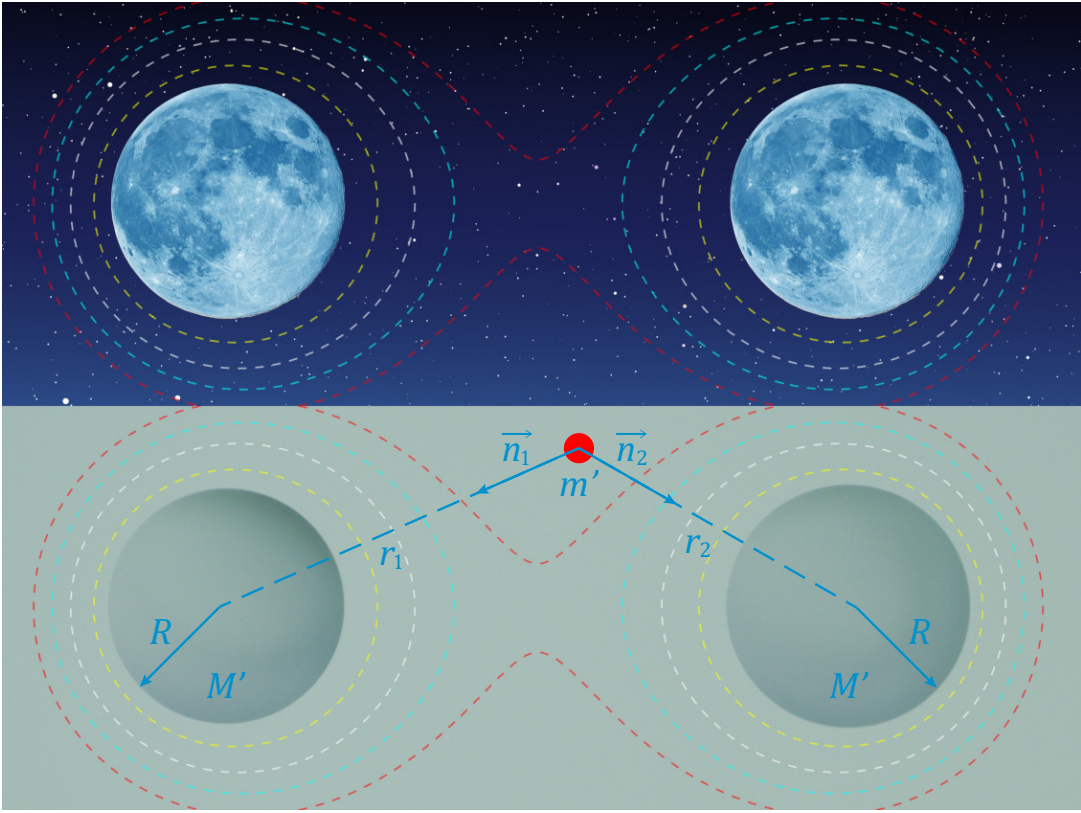


FIG. 5. (Top) Gravitational equipotential lines between two celestial bodies. From outside to inside, the gravitational potentials represented are  $E_0$ ,  $1.09E_0$ ,  $1.20E_0$  and  $1.38E_0$ , respectively. (Bottom) Humidity equipotential lines between two 10 wt% PG droplets on a high energy substrate. From outside to inside, the humidity potentials represented are  $E'$ ,  $1.09E'$ ,  $1.20E'$  and  $1.38E'$ , respectively.

To conclude, we discover a new inverse-square law force between vapor-mediated droplets. We believe it will apply to broader systems beyond what have been investigated here, and will be highly beneficial to droplet research and applications. With a clear-cut “propagator”, the problem studied here could provide new perspectives for a better understanding of inverse square laws.

This study was supported by the National Natural Science Foundation of China (11972339, 11772327, 11932019, 11621202), the Fundamental Research Funds for the Central Universities (WK2090000023), and the Strategic Priority Research Program of the Chinese Academy of Sciences (XDB22040403).

- 
- [1] I. Newton, *Philosophiæ naturalis principia mathematica* (*Mathematical principles of natural philosophy*), London (1687).
  - [2] C. A. de Coulomb, Premier mémoire sur l’électricité et le magnétisme, Histoire de l’Académie Royale des Sciences, 569 (1785).
  - [3] R. M. Wald, *General relativity*, University of Chicago Press, Chicago, USA, (1984).
  - [4] W. Greiner and J. Reinhardt, *Quantum electrodynamics*, Springer-Verlag, Berlin, Heidelberg, (2003).
  - [5] N. J. Ciria, A. Benusiglio, and M. Prakash, Vapour-mediated sensing and motility in two-component droplets, *Nature* **519**, 446 (2015).
  - [6] V. Paunov, P. Kralchevsky, N. Denkov, and K. Nagayama, Lateral capillary forces between floating submillimeter particles, *Journal of Colloid and Interface Science* **157**, 100 (1993).
  - [7] D. Vella and L. Mahadevan, The “cheerios effect”, *American Journal of Physics* **73**, 817 (2005).
  - [8] P. A. Kralchevsky and K. Nagayama, Capillary interactions between particles bound to interfaces, liquid films and biomembranes, *Advances in Colloid and Interface Science* **85**, 145 (2000).
  - [9] S. Karpitschka, A. Pandey, L. A. Lubbers, J. H. Weijs, L. Botto, S. Das, B. Andreotti, and J. H. Snoeijer, Liquid drops attract or repel by the inverted cheerios effect, *Proceedings of the National Academy of Sciences* **113**, 7403 (2016).
  - [10] R. D. Deegan, O. Bakajin, T. F. Dupont, G. Huber, S. R. Nagel, and T. A. Witten, Capillary flow as the cause of ring stains from dried liquid drops, *Nature* **389**, 827 (1997).

- [11] P.-G. De Gennes, F. Brochard-Wyart, and D. Quéré, *Capillarity and wetting phenomena: drops, bubbles, pearls, waves*, Springer, New York, (2003).
- [12] D. Lohse and X. Zhang, Physicochemical hydrodynamics of droplets out of equilibrium, *Nature Reviews Physics* **2**, 426 (2020).
- [13] P. J. Yunker, T. Still, M. A. Lohr, and A. Yodh, Suppression of the coffee-ring effect by shape-dependent capillary interactions, *Nature* **476**, 308 (2011).
- [14] Y. Li, C. Diddens, P. Lv, H. Wijshoff, M. Versluis, and D. Lohse, Gravitational effect in evaporating binary microdroplets, *Physical Review Letters* **122**, 114501 (2019).
- [15] Y. Li, C. Diddens, T. Segers, H. Wijshoff, M. Versluis, and D. Lohse, Evaporating droplets on oil-wetted surfaces: Suppression of the coffee-stain effect, *Proceedings of the National Academy of Sciences* **117**, 16756 (2020).
- [16] H. Sadafi, S. Dehaeck, A. Rednikov, and P. Colinet, Vapor-mediated versus substrate-mediated interactions between volatile droplets, *Langmuir* **35**, 7060 (2019).
- [17] S. Daniel, Fast Drop Movements Resulting from the Phase Change on a Gradient Surface, *Science* **291**, 633 (2001).
- [18] X. Man and M. Doi, Vapor-induced motion of liquid droplets on an inert substrate, *Physical Review Letters* **119**, 044502 (2017).
- [19] Y. Wen, P. Y. Kim, S. Shi, D. Wang, X. Man, M. Doi, and T. P. Russell, Vapor-induced motion of two pure liquid droplets, *Soft Matter* **15**, 2135 (2019).
- [20] H. Hu and R. G. Larson, Analysis of the effects of marangoni stresses on the microflow in an evaporating sessile droplet, *Langmuir* **21**, 3972 (2005).
- [21] S. Karpitschka, F. Liebig, and H. Riegler, Marangoni contraction of evaporating sessile droplets of binary mixtures, *Langmuir* **33**, 4682 (2017).
- [22] R. Malinowski, I. P. Parkin, and G. Volpe, Nonmonotonic contactless manipulation of binary droplets via sensing of localized vapor sources on pristine substrates, *Science Advances* **6**, eaba3636 (2020).
- [23] F. Brochard, Motions of droplets on solid surfaces induced by chemical or thermal gradients, *Langmuir* **5**, 432 (1989).
- [24] H. Hu and R. G. Larson, Evaporation of a sessile droplet on a substrate, *The Journal of Physical Chemistry B* **106**, 1334 (2002).
- [25] R. L. Hoffman, A study of the advancing interface. I. Interface shape in liquid—gas systems, *Journal of Colloid and Interface Science* **50**, 228 (1975).
- [26] O. Voinov, Hydrodynamics of wetting, *Fluid Dynamics* **11**, 714 (1976).
- [27] R. Cox, The dynamics of the spreading of liquids on a solid surface. part 1. viscous flow, *Journal of Fluid Mechanics* **168**, 169 (1986).
- [28] E. Reyssat, Drops and bubbles in wedges, *Journal of Fluid Mechanics* **748**, 641 (2014).
- [29] S. Shiri, S. Sinha, D. A. Baumgartner, and N. J. Cira, Thermal marangoni flow impacts the shape of single component volatile droplets on thin, completely wetting substrates, *Physical Review Letters* **127**, 024502 (2021).
- [30] D. Liu and T. Tran, Vapor-induced attraction of floating droplets, *The Journal of Physical Chemistry Letters* **9**, 4771 (2018).



**Supplementary Information to:  
The Inverse-Square Law Force between  
Vapor-Mediated Droplets**

### I. MATERIALS AND EXPERIMENTS.

	Density $\rho$ (kg m <sup>-3</sup> )	Surface Tension $\gamma$ (mN m <sup>-1</sup> )	Dynamic Viscosity $\mu$ (mPa·s)
air	1.20	—	0.018
water	998	72.7	1.0
PG	1038	35.7	56.0
10 wt% PG aqueous solution	1005	59.2	1.4
20 wt% PG aqueous solution	1014	55.7	2.0
40 wt% PG aqueous solution	1032	47.8	4.6
60 wt% PG aqueous solution	1043	38.7	9.4

TAB. SI. Properties of the liquids used in the experiments. All values were measured at room temperature of 20 °C.

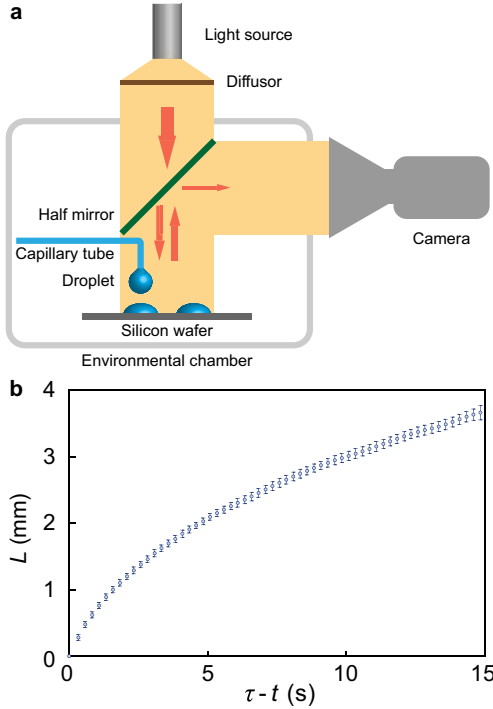


FIG. S1. (a) Sketch of the experimental configuration, showing the capillary micro-tube used to pinch off the droplet. (b) Mean distance between droplets as a function of time before contact for two moving 10 wt% PG droplets.  $R = 1.37 \pm 0.02$  mm and  $\phi_\infty = 51.3\% \pm 2.0\%$ . The error bars represent the standard deviation of 10 experiments.

### II. HUMIDITY DISTRIBUTION AROUND A SESSILE DROPLET.

The evaporation process of droplets is a diffusion process, and the relative air humidity  $\phi$  satisfies the diffusion equation,

$$\frac{\partial \phi}{\partial t} = D \nabla^2 \phi, \quad (\text{S1})$$

where  $D = 26.1 \text{ mm}^2 \text{ s}^{-1}$  is the diffusion coefficient [1]. In our experiments, the characteristic length  $R \sim 1$  mm, characteristic time is  $t_c \sim 1$  s, leading to a diffusion time scale  $t_d = R^2/D = 0.04 \text{ s} \ll t_c$ . Therefore, droplet motion can be treated as a quasi-static process, during which Eq. S1 can be simplified as Laplace's equation  $D \nabla^2 \phi = 0$ . In spherical coordinates it reads

$$\frac{1}{r^2} \frac{\partial}{\partial r} \left( r^2 \frac{\partial \phi}{\partial r} \right) = 0, \quad (\text{S2})$$

$\phi(R) = 1$ ,  $\phi(\infty) = \phi_\infty$ , where  $R$  is droplet radius,  $\phi_\infty$  is the ambient humidity in the far field. The centrosymmetric solution for  $\phi$  around a spherical droplet with an infinity boundary reads

$$\phi(r) = \frac{(1 - \phi_\infty)R}{r} + \phi_\infty. \quad (\text{S3})$$

For evaporation from a sessile droplet on a solid substrate, we can write the droplet profile for a spherical cap

$$h(r) = \sqrt{R^2 / \sin^2 \theta - r^2} - R / \tan \theta, \quad (\text{S4})$$

and the boundary conditions

$$\begin{aligned} r < R, z = h(r) : \phi &= 1; \\ r > R, z = 0 : J &= 0; \\ r = \infty, z = \infty : \phi &= \phi_\infty, \end{aligned} \quad (\text{S5})$$

where  $J$  is the evaporation flux,  $\theta$  is the contact angle,  $h$ ,  $r$  and  $z$  are geometric parameters, as shown in Fig. S2a. In toroidal coordinate, the Laplace equation  $\nabla^2 \phi = 0$  has an analytical solution

$$\begin{aligned} \frac{\phi - \phi_\infty}{1 - \phi_\infty} &= \sqrt{2 \cosh \alpha - 2 \cos \beta}. \\ \int_0^\infty \frac{\cosh(\theta \omega)}{\cosh(\pi \omega)} \frac{\cosh[(2\pi - \beta)\omega]}{\cosh[(\pi - \theta)\omega]} P_{-1/2+i\pi}(\cosh \alpha) d\omega, \end{aligned} \quad (\text{S6})$$

where  $P_{-1/2+i\pi}(\cosh \alpha)$  is the Legendre function of the first kind.

$$\begin{aligned} P_{-1/2+i\pi}(\cosh \alpha) &= \frac{2}{\pi} \coth(\pi \omega) \int_\alpha^\infty \frac{\sin(\omega t)}{\sqrt{2 \cosh t - 2 \cosh \alpha}} dt. \end{aligned} \quad (\text{S7})$$

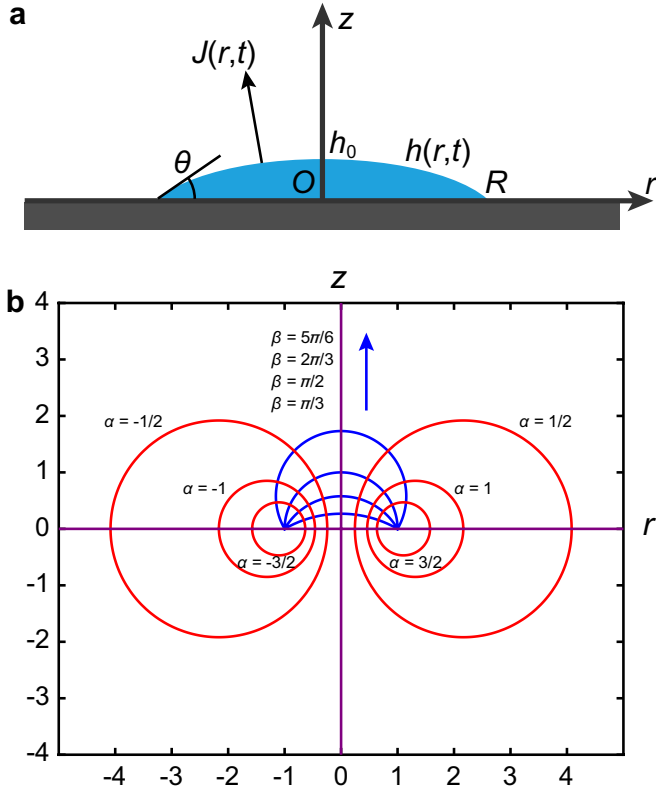


FIG. S2. Schematic showing the evaporation of a sessile droplet in (a) cylindrical coordinate system and (b) toroidal coordinate system.

The toroidal coordinates  $\alpha$  and  $\beta$  (Fig. S2b) are related to the cylindrical coordinates  $r$  and  $z$  by

$$\begin{aligned} r &= \frac{R \sinh \alpha}{\cosh \alpha - \cos \beta}, \\ z &= \frac{R \sin \beta}{\cosh \alpha - \cos \beta}. \end{aligned} \quad (\text{S8})$$

For a thin liquid film with  $\theta = 0$ , Eq. S6 is reduced to

$$\begin{aligned} \frac{\phi - \phi_\infty}{1 - \phi_\infty} &= \frac{1}{2} - \frac{1}{\pi} \arctan \left[ \frac{\cos \beta - \sinh^2(\alpha/2)}{\cos(\beta/2) \sqrt{2 \cosh \alpha - 2 \cos \beta}} \right]. \end{aligned} \quad (\text{S9})$$

For humidity distribution along the solid substrate, i.e.,  $z = 0$ , Eq. S9 is further reduced to

$$\frac{\phi - \phi_\infty}{1 - \phi_\infty} = \frac{1}{2} - \frac{1}{\pi} \arctan \left[ \frac{1 - \sinh^2(\alpha/2)}{\sqrt{2 \cosh \alpha - 2}} \right]. \quad (\text{S10})$$

From Eq. S8 we get  $\sinh(\alpha/2) = \sqrt{1/(r^2/R^2 - 1)}$ . Denoting  $\tilde{r}$  as  $\tilde{r} = r/R$ , the arctangent term in Eq. S10 can

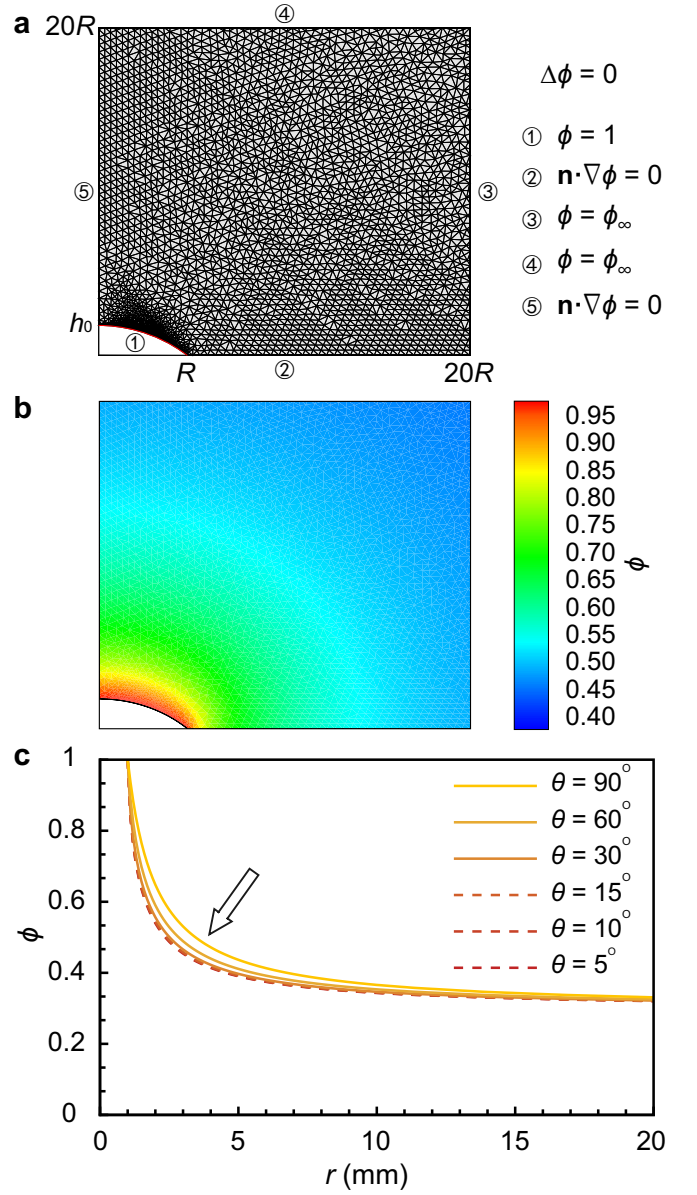


FIG. S3. (a) Mesh partition and boundary conditions for finite element calculation of  $\phi$ . (b) Calculated humidity field of an evaporating sessile droplet.  $\phi_\infty = 30\%$ ,  $\theta = 38^\circ$ . (c) Dependence of  $\phi$  on  $\theta$ . Different curves of  $\phi$  converge to a single curve when  $\theta \leq 30^\circ$ . Arrows marks the direction of convergence.

be expressed as

$$\begin{aligned} f(\tilde{r}) &= \arctan \left[ \frac{1 - \sinh^2(\alpha/2)}{\sqrt{2 \cosh \alpha - 2}} \right] \\ &= \arctan \left[ \frac{1 - \sinh^2(\alpha/2)}{2 \sinh(\alpha/2)} \right] \\ &= \arctan \left[ \frac{1 - 1/(\tilde{r}^2 - 1)}{2 \sqrt{1/(\tilde{r}^2 - 1)}} \right]. \end{aligned} \quad (\text{S11})$$

The asymptotic expansion of  $f(\tilde{r})$  at infinity reads

$$f(\tilde{r}) = \frac{\pi}{2} - \frac{2}{\tilde{r}} - \frac{1}{3\tilde{r}^3} - \frac{3}{20\tilde{r}^5} + O\left[\frac{1}{\tilde{r}}\right]^6. \quad (\text{S12})$$

Consider the correction to the first-order term by the higher-order term with least square fit, we get

$$f(\tilde{r}) = \frac{\pi}{2} - \frac{2.2}{\tilde{r}}. \quad (\text{S13})$$

Eventually, the humidity distribution of sessile droplet along the substrate reads

$$\phi(r) = \frac{\lambda(1 - \phi_\infty)R}{r} + \phi_\infty, \quad (\text{S14})$$

where  $\lambda = 2.2/\pi \approx 0.7$ .

To verify our inference, Finite element method software FreeFem++ was also used to solve the Laplace equation. The computational domain and numerical results are shown in Fig. S3. Fig. S3c shows the dependence of  $\phi$  on  $\theta$ . It is shown that different curves of  $\phi$  collapse into a single curve when  $\theta < 30^\circ$ . For our experiments where  $\theta \in [5^\circ, 15^\circ]$ , the influence of contact angle on humidity distribution is negligible. Therefore, we could use Eq. S10 or Eq. S14 to estimate humidity distribution  $\phi$ . In the main text, a comparison among theoretical result, asymptotic solution, and numerical result is shown in Fig. 2b.

### III. DEPENDENCE OF CONTACT ANGLE ON HUMIDITY.

Different models have been used to predict humidity's effects on the contact angle of a sessile droplet on a solid substrate. For example [2, 3],

$$\cos \theta = m_l \phi + b_l, \quad (\text{S15})$$

$$\theta = m_t (\phi_{eq} - \phi)^{1/3}, \quad (\text{S16})$$

and the model we propose in the main text,

$$\cos \theta = \frac{1}{2} m_p \phi^2 + b_p, \quad (\text{S17})$$

where  $\phi_{eq}$  is the equilibrium relative humidity when the droplet spreads completely, and  $m_l$ ,  $b_l$ ,  $m_t$ ,  $m_p$ ,  $b_p$  are fitting parameters.

A comparison between experimental data and results obtained from three different models is shown in Fig. S4, where  $m_p = 0.065$  and  $b_p = 0.97$ ,  $m_l = 0.036$  and  $b_l = 0.96$ ,  $m_t = 0.28$  and  $\phi_{eq} = 0.95$ , respectively.

### IV. DRIVEN FORCE BETWEEN EVAPORATING SESSILE DROPLETS.

Microscopic observation of the binary droplets revealed a thin film extending tens of microns from the edge of

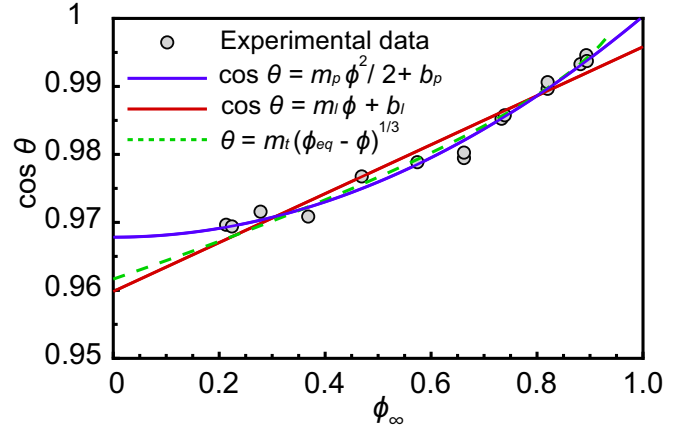


FIG. S4. Contact angle as a function of  $\phi_\infty$  for a 10 wt% PG droplet on a hydrophilic silicon surface. The fitting coefficients are  $m_p = 0.065$  and  $b_p = 0.97$ ,  $m_l = 0.036$  and  $b_l = 0.96$ ,  $m_t = 0.28$  and  $\phi_{eq} = 0.95$ , for three different models, respectively.

the bulk droplet [2]. The Young equation indicates that  $\gamma = \gamma_d \cos \theta$ , where  $\gamma$  is surface tension along the periphery of the “target” droplet, and  $\gamma_d$  is surface tension of droplet. As mentioned above, contact angle is a function of humidity  $\cos \theta = f(\phi)$ . To simplify the analysis,  $\cos \theta$  is expanded linearly,

$$\cos \theta = f'(\phi_\infty)(\phi - \phi_\infty) + f(\phi_\infty) = m\phi + b, \quad (\text{S18})$$

where  $m = f'(\phi_\infty)$  and  $b = -f'(\phi_\infty)\phi_\infty + f(\phi_\infty)$ . For the case shown in Fig. 2b in the main text, the calculated relative error at distance  $r = 2R$  (corresponding to  $L = 0$ ) is 1.49%, verifying the feasibility of the linear approximation. Resultant force exerted on the “target” droplet is

$$\begin{aligned} F &= \int_0^{2\pi} \gamma \cos \varphi R d\varphi \\ &= \int_0^{2\pi} \gamma_d \cos \theta \cos \varphi R d\varphi \\ &= \int_0^{2\pi} \gamma_d (m\phi + b) \cos \varphi R d\varphi \\ &= \gamma_d m_p \phi_\infty R \int_0^{2\pi} \phi \cos \varphi d\varphi \\ &= \gamma_d m_p \phi_\infty R \int_0^{2\pi} \left[ \frac{\lambda(1 - \phi_\infty)R}{r} + \phi_\infty \right] \cos \varphi d\varphi \\ &= \gamma_d m_p \phi_\infty \lambda R^2 (1 - \phi_\infty) \int_0^{2\pi} \frac{\cos \varphi}{r} d\varphi. \end{aligned} \quad (\text{S19})$$

Introducing a relatively small variable  $\epsilon_1 = R/(L + 2R)$  where  $0 < \epsilon_1 < 1/2$ ,

$$\begin{aligned} \frac{1}{r} &= \frac{1}{\sqrt{(L + 2R + R \cos \varphi)^2 + (R \sin \varphi)^2}} \\ &= \frac{1}{L + 2R} \frac{1}{\sqrt{1 + 2\epsilon_1 \cos \varphi + \epsilon_1^2}} \\ &= \frac{1}{L + 2R} \sum_{n=0}^{\infty} P_n(-\cos \varphi) \epsilon_1^n \\ &\approx \frac{1}{L + 2R} \left[ 1 - \epsilon_1 \cos \varphi + \frac{\epsilon_1^2}{2} (3 \cos^2 \varphi - 1) \right. \\ &\quad \left. + \frac{\epsilon_1^3}{2} (-5 \cos^3 \varphi + 3 \cos \varphi) + o(\epsilon_1^3) \right], \end{aligned} \quad (\text{S20})$$

where  $P_n$  is the Legendre polynomial of order  $n$ . Thereby we have

$$\begin{aligned} &\int_0^{2\pi} \frac{\cos \varphi}{r} d\varphi \\ &\approx \frac{1}{L + 2R} \int_0^{2\pi} \cos \varphi \left[ 1 - \epsilon_1 \cos \varphi + \frac{\epsilon_1^2}{2} (3 \cos^2 \varphi - 1) \right. \\ &\quad \left. + \frac{\epsilon_1^3}{2} (-5 \cos^3 \varphi + 3 \cos \varphi) \right] d\varphi \\ &= -\frac{\pi R}{(L + 2R)^2} - \frac{3\pi R^3}{8(L + 2R)^4}. \end{aligned} \quad (\text{S21})$$

Ignoring higher-order terms, the resultant force of third-order accuracy can be expressed as

$$F = -\frac{\gamma_d m_p \phi_\infty \lambda \pi R^3 (1 - \phi_\infty)}{(L + 2R)^2}. \quad (\text{S22})$$

The residual is  $3\epsilon_1^2/8 < 5\%$  when  $L > R$ .

## V. DRAG OF A MOVING DROPLET.

When a droplet moves on the silicon wafer, drag  $F_d = F_{cl} + F_{bulk}$ , where  $F_{cl}$  and  $F_{bulk}$  originates from moving contact line and the wetting area, respectively [4]. In the vicinity of contact line, previous works show that the local velocity of the droplet liquid is perpendicular to the contact line [5, 6], as shown in Fig. S5. The drag  $f$  exerted on per unit contact line length is

$$f = \frac{3\mu l_n v}{\theta} = \frac{3\mu l_n U \cos \varphi}{\theta}, \quad (\text{S23})$$

where  $\mu$  is dynamic viscosity of liquid,  $v$  is the local velocity of contact line,  $\theta$  is dynamical contact angle,  $l_n = \ln(l_{max}/l_{min})$  is the logarithmic cut-off coefficient [7],  $l_{max}$  is the macroscopic characteristic length and  $l_{min}$  is the microscopic characteristic length, respectively. Generally,  $l_n \approx 15$  for droplet moving on a dry surface [8] and  $l_n \approx 5$  for droplet moving on a wet surface [4].

For constant  $\theta$  during droplet motion, the drag originating from contact line can be derived by integrating Eq. S23 along the contact line,

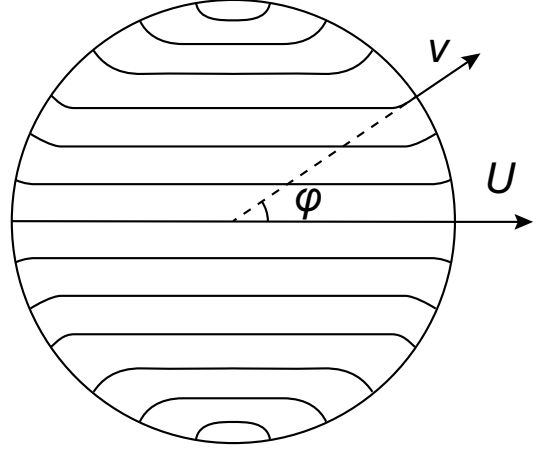


FIG. S5. The local velocity of the droplet liquid is perpendicular to the contact line. A copy sketch to fig. 2b from [9].

$$\begin{aligned} F_{cl} &= \int_0^{2\pi} f \cos \varphi R d\varphi \\ &= \int_0^{2\pi} \frac{3\mu l_n R U \cos^2 \varphi}{\theta} d\varphi \\ &= \frac{3\pi \mu l_n R U}{\theta}. \end{aligned} \quad (\text{S24})$$

$F_{bulk}$  can be estimated as

$$F_{bulk} \sim \frac{\mu U}{h} \pi R^2 = \frac{\mu U}{R\theta} \pi R^2 = \frac{\mu \pi R U}{\theta}, \quad (\text{S25})$$

where  $h \approx R\theta$  is the height of the sessile droplet. Comparing Eq. S24 and S25,  $F_{cl}/F_{bulk} \sim 3l_n \gg O(1)$ , therefore drag  $F_{bulk}$  is negligible and the total drag of droplet reads

$$F_d = \frac{3\pi \mu l_n R U}{\theta}. \quad (\text{S26})$$

If the dynamic contact angle changes with droplet velocity, the classical Cox-Voinov law gives

$$\theta^3 = \theta_m^3 + 9l_n Ca, \quad (\text{S27})$$

where  $\theta_m$  is the microscopic contact angle and  $Ca = \mu U/\gamma$  is the capillary number. Due to the existence of a thin liquid film around the edge of droplet in our experiments, we have  $\theta_m = 0$ , and the Cox-Voinov law can be simplified to Tanner's law which gives  $\theta \sim Ca^{1/3}$ . Consequently Eq. S24 and Eq. S25 will be reduced to

$$F'_{cl} = \frac{3\pi \mu l_n R U}{\theta} \sim \frac{\gamma R C a}{C a^{1/3}} = \gamma R C a^{2/3} \quad (\text{S28})$$

and

$$F'_{bulk} \sim \frac{\pi \mu U R^2}{h} = \frac{\pi \mu U R}{\theta} \sim \gamma R C a^{2/3}, \quad (\text{S29})$$

respectively. The total drag reads

$$F'_d = F'_{cl} + F'_{bulk} \sim \gamma R C a^{2/3}. \quad (\text{S30})$$

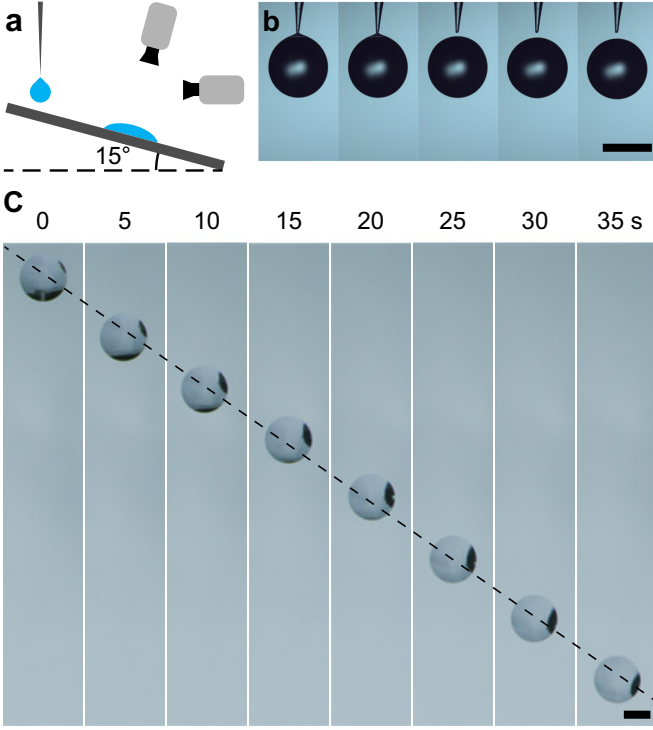


FIG. S6. (a) The sketch of a droplet sliding along a silicon wafer with an inclination angle of  $15^\circ$ . (b) The pinch-off of a 10 wt% PG aqueous droplet from a conical capillary tube. Scale bar is 1 mm. (c) Droplet sliding down along a silicon wafer with an inclination angle of  $15^\circ$ . The droplet has reached its terminal velocity. scale bar is 2 mm.

To verify above analysis, systematic experiments were conducted for droplet sliding down process along a tilt silicon wafer with an inclination angle of  $15^\circ$ . The driving force is the gravity force component along the substrate

$$F_g = \rho \Omega g \sin 15^\circ, \quad (\text{S31})$$

where  $\rho$  is the liquid density,  $\Omega$  is the droplet volume and  $g$  is the gravity acceleration, respectively.  $\rho$  was measured by a side-view high-speed camera, and the droplet sliding process was observed by another high-speed camera perpendicular to substrate (Fig. S6a). When the droplet reaches its terminal velocity,  $F_g$  is balanced by  $F_d$ . Comparing Eq. S26, S30 and Eq. S31, we obtain two expressions

$$\rho \Omega g \sin 15^\circ = \frac{3\pi\mu l_n R U_t}{\theta}, \quad (\text{S32})$$

$$\rho \Omega g \sin 15^\circ = k_d \gamma R C a_t^{2/3}, \quad (\text{S33})$$

where  $U_t$  is terminal velocity,  $C a_t = \mu U_t / \gamma$  and  $k_d$  is a fitting coefficient, respectively. Feasibility of Eqs. S32 and S33 were tested in Fig. 3a in the main text. The experimental data fits better with Eq. S26 and the best fit gives  $l_n = 17.8$ .

## VI. EFFECTS OF DROPLET DEFORMATION ON ITS MOTION.

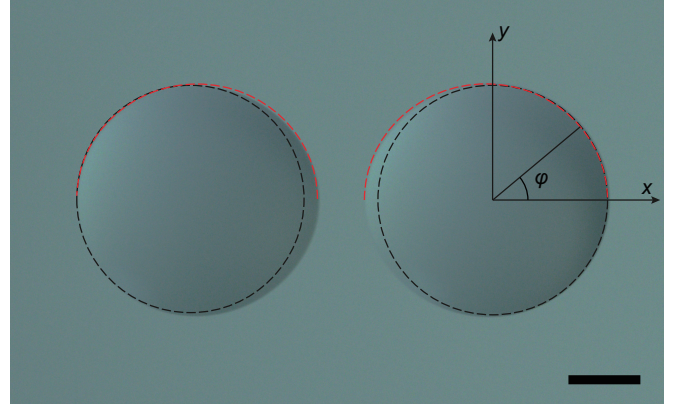


FIG. S7. Small deformation of adjacent 10 wt% PG aqueous droplets 0.1 s before contact. The semicircle composed of red broken lines is used to mark the outline of the droplet. Scale bar is 1 mm.

Just before contact, droplets will undergo a small deformation, as shown in Fig. S7. Below we will investigate its effects on the driving force  $F$  that exerted on droplet.

For a small deformation, the drag at the receding contact line keeps constant as

$$\begin{aligned} F_d^r &= 2 \int_0^{\pi/2} f_r \cos \varphi R d\varphi \\ &= 2 \int_0^{\pi/2} \frac{3\mu l_n R U \cos^2 \varphi}{\theta} d\varphi \\ &= \frac{3\pi\mu l_n R U}{2\theta}, \end{aligned} \quad (\text{S34})$$

where  $f_r$  denotes the drag exerted on per unit advancing contact line length.

At the advancing contact line, the deformation of the droplet can be expressed with  $r = R[1 + \epsilon_2 f(\varphi)]$  in polar coordinates (Fig. S7) where  $\epsilon_2 < 0.1$  is a negligible constant. With  $x = r(\varphi) \cos \varphi$  and  $y = r(\varphi) \sin \varphi$ , the tangent vector of the advancing contact line can be expressed as

$$\mathbf{T} = \left[ \frac{dx}{d\varphi}, \frac{dy}{d\varphi} \right]^T, \quad (\text{S35})$$

and the unit tangent vector and the unit normal vector can be expressed as

$$\mathbf{t} = \mathbf{T} / \|\mathbf{T}\|, \quad \mathbf{n} = \mathbf{A} \cdot \mathbf{t}, \quad \mathbf{A} = \begin{bmatrix} 0 & 1 \\ -1 & 0 \end{bmatrix}, \quad (\text{S36})$$

where

$$\mathbf{t} = \begin{bmatrix} -\sin \varphi + \epsilon_2 \cos \varphi f'(\varphi) + \epsilon_2^2 [\sin \varphi f'(\varphi)^2/2 \\ -f(\varphi)f'(\varphi) \cos \varphi] + o(\epsilon_2^2), \\ \cos \varphi + \epsilon_2 \sin \varphi f'(\varphi) + \epsilon_2^2 [-\cos \varphi f'(\varphi)^2/2 \\ -f(\varphi)f'(\varphi) \sin \varphi] + o(\epsilon_2^2) \end{bmatrix}^T, \quad (\text{S37})$$

$$\mathbf{n} = \begin{bmatrix} \cos \varphi + \epsilon_2 \sin \varphi f'(\varphi) + \epsilon_2^2 [-\cos \varphi f'(\varphi)^2/2 \\ -f(\varphi)f'(\varphi) \sin \varphi] + o(\epsilon_2^2), \\ \sin \varphi - \epsilon_2 \cos \varphi f'(\varphi) + \epsilon_2^2 [-\sin \varphi f'(\varphi)^2/2 \\ +f(\varphi)f'(\varphi) \cos \varphi] + o(\epsilon_2^2) \end{bmatrix}^T. \quad (\text{S38})$$

Denoting the drag per unit advancing contact line length as  $f_a = 3\mu l_n U n_x / \theta$ , and arc length element as

$$ds = \sqrt{r^2 + r'^2} d\varphi \\ = R[1 + \epsilon_2 f(\varphi) + \epsilon_2^2 f'^2(\varphi)/2 + o(\epsilon_2^2)] d\varphi, \quad (\text{S39})$$

where  $n_x$  is the  $x$  component of unit normal vector and  $r' = dr/d\varphi$ , the drag at the advancing contact line reads

$$F_d^a = 2 \int_{\pi/2}^{\pi} f_a n_x ds \\ = 2 \int_{\pi/2}^{\pi} \frac{3\mu l_n U n_x^2}{\theta} ds \\ = \frac{6\mu l_n U}{\theta} \int_{\pi/2}^{\pi} n_x^2 ds \\ \approx \frac{6\mu l_n R U}{\theta} \int_{\pi/2}^{\pi} [\cos^2 \varphi + \epsilon_2 \sin 2\varphi f'(\varphi) \\ + \epsilon_2 \cos^2 \varphi f(\varphi)] d\varphi. \quad (\text{S40})$$

For the integral in the above formula,

$$I = \int_{\pi/2}^{\pi} [\cos^2 \varphi + \epsilon_2 \sin 2\varphi f'(\varphi) + \epsilon_2 \cos^2 \varphi f(\varphi)] d\varphi \\ = \frac{\pi}{4} + \epsilon_2 \int_{\pi/2}^{\pi} \sin 2\varphi f'(\varphi) d\varphi + \epsilon_2 \int_{\pi/2}^{\pi} \cos^2 \varphi f(\varphi) d\varphi \\ = \frac{\pi}{4} - 2\epsilon_2 \int_{\pi/2}^{\pi} \cos 2\varphi f(\varphi) d\varphi + \epsilon_2 \int_{\pi/2}^{\pi} \cos^2 \varphi f(\varphi) d\varphi, \quad (\text{S41})$$

and the boundary condition  $f(\pi/2) = 0$ ,  $f(\pi) = 1$ . Assuming that  $f(\pi)$  is a linear function, the integral can be reduced to

$$I \approx \frac{\pi}{4} - \frac{2\epsilon_2}{\pi} + \epsilon_2 \left( \frac{1}{2\pi} + \frac{\pi}{8} \right) = \frac{\pi}{4} - \epsilon_2 \left( \frac{3}{2\pi} - \frac{\pi}{8} \right). \quad (\text{S42})$$

Therefore the total drag is

$$F_d = F_d^r + F_d^a = \frac{3\pi\mu l_n R U}{\theta} \left[ 1 - \epsilon_2 \left( \frac{3}{\pi^2} - \frac{1}{4} \right) \right] \\ \approx \frac{3\pi\mu l_n R U}{\theta} \left( 1 - \frac{\epsilon_2}{20} \right). \quad (\text{S43})$$

Next we investigate the resultant driving force  $F$  when droplet deformation is involved in. The resultant force at the receding contact line reads

$$F^r = 2 \int_0^{\pi/2} [\gamma_0 + \Gamma r(\varphi) \cos \varphi] \cos \varphi R d\varphi \\ = \pi R^2 \Gamma / 2 + 2\gamma_0 R, \quad (\text{S44})$$

and the resultant force at the advancing contact line is

$$F^a = 2 \int_{\pi/2}^{\pi} \gamma n_x ds \\ = 2 \int_{\pi/2}^{\pi} [\gamma_0 + \Gamma r(\varphi) \cos \varphi] n_x ds \\ \approx 2R \int_{\pi/2}^{\pi} (\gamma_0 \cos \varphi + \Gamma R \cos^2 \varphi) d\varphi \\ + 2R \int_{\pi/2}^{\pi} \epsilon_2 [\gamma_0 f(\varphi) \cos \varphi + \gamma_0 f'(\varphi) \sin \varphi] d\varphi \\ + 2R \int_{\pi/2}^{\pi} \epsilon_2 [2\Gamma R \cos^2 \varphi f(\varphi) \\ + \Gamma R \cos \varphi \sin \varphi f'(\varphi)] d\varphi \\ = -2\gamma_0 R + \pi R^2 (1 + \epsilon_2) \Gamma / 2. \quad (\text{S45})$$

Hence the resultant driving force reads

$$F = F^r + F^a = \pi R^2 \Gamma (1 + \epsilon_2 / 2). \quad (\text{S46})$$

The surface tension gradient of the droplet is

$$\Gamma \sim \frac{1}{(L + 2R + R\epsilon_2)^2} \\ = \frac{1}{(L + 2R)^2} \frac{1}{[1 + R\epsilon_2/(L + 2R)]^2} \\ = \frac{1}{(L + 2R)^2} \left[ 1 - \frac{2R\epsilon_2}{L + 2R} + o(\epsilon_2) \right], \quad (\text{S47})$$

and we can get  $\Gamma = \Gamma_0(1 - \epsilon_2)$  and total resultant force

$$F = \pi R^2 \Gamma_0 (1 + \epsilon_2 / 2) (1 - \epsilon_2) \approx \pi R^2 \Gamma_0 (1 - \epsilon_2 / 2), \quad (\text{S48})$$

where  $\Gamma_0$  denotes surface tension gradient for the droplet without deformation. Comparing two cases with and without droplet deformation,

$$\pi R^2 \Gamma_0 = \frac{3\pi\mu l_n R U_0}{\theta}, \\ \pi R^2 \Gamma_0 (1 - \frac{\epsilon_2}{2}) = \frac{3\pi\mu l_n R U}{\theta} \left( 1 - \frac{\epsilon_2}{20} \right), \quad (\text{S49})$$

we get  $U/U_0 = (1 - \epsilon_2/2)/(1 - \epsilon_2/20) \approx 1 - 9\epsilon_2/20$ , where  $U_0$  denotes velocity of the droplet without deformation. Finally, the change in velocity due to small deformation of droplet is  $|(U - U_0)/U_0| < 5\%$ , which is negligible.



## VII. DRIVEN FORCE BETWEEN EVAPORATING DROPLETS WITH DIFFERENT RADIUS RATIOS.

When the “source” and “target” droplets are different in size (Fig. S8), the resultant driving force on “target” droplet reads

$$\begin{aligned}
 F &= \int_0^{2\pi} \gamma \cos \varphi R_2 d\varphi \\
 &= \int_0^{2\pi} \gamma_d \cos \theta \cos \varphi R_2 d\varphi \\
 &= \int_0^{2\pi} \gamma_d (m\phi + b) \cos \varphi R_2 d\varphi \\
 &= \gamma_d m_p \phi_\infty R_2 \int_0^{2\pi} \phi \cos \varphi d\varphi, \quad (\text{S50})
 \end{aligned}$$

substituting  $\phi = \lambda(1 - \phi_\infty)R_1/r + \phi_\infty$ , we get

$$\begin{aligned}
 F &= \gamma_d m_p \phi_\infty R_2 \int_0^{2\pi} \left[ \frac{\lambda(1 - \phi_\infty)R_1}{r} + \phi_\infty \right] \cos \varphi d\varphi \\
 &= \gamma_d m_p \phi_\infty \lambda R_1 R_2 (1 - \phi_\infty) \int_0^{2\pi} \frac{\cos \varphi}{r} d\varphi. \quad (\text{S51})
 \end{aligned}$$

We introduce  $\epsilon_3 = R_2/(L + R_1 + R_2)$  to simplify  $1/r$

$$\begin{aligned}
 \frac{1}{r} &= \frac{1}{\sqrt{(L + R_1 + R_2 + R_2 \cos \varphi)^2 + (R_2 \sin \varphi)^2}} \\
 &= \frac{1}{L + R_1 + R_2} \frac{1}{\sqrt{1 + 2\epsilon_3 \cos \varphi + \epsilon_3^2}} \\
 &= \frac{1}{L + R_1 + R_2} \sum_{n=0}^{\infty} P_n(-\cos \varphi) \epsilon_3^n \\
 &= \frac{1}{L + R_1 + R_2} \left[ 1 - \epsilon_3 \cos \varphi + \frac{\epsilon_3^2}{2} (3 \cos^2 \varphi - 1) \right. \\
 &\quad \left. + \frac{\epsilon_3^3}{2} (-5 \cos^3 \varphi + 3 \cos \varphi) + o(\epsilon_3^3) \right] \\
 &\approx \frac{1}{L + R_1 + R_2} \left[ 1 - \epsilon_3 \cos \varphi + \frac{\epsilon_3^2}{2} (3 \cos^2 \varphi - 1) \right. \\
 &\quad \left. + \frac{\epsilon_3^3}{2} (-5 \cos^3 \varphi + 3 \cos \varphi) \right]. \quad (\text{S52})
 \end{aligned}$$

Hence the integral item  $\int_0^{2\pi} \cos \varphi / r d\varphi$  reads

$$\begin{aligned}
 \int_0^{2\pi} \frac{\cos \varphi}{r} d\varphi &\approx \frac{1}{L + R_1 + R_2} \int_0^{2\pi} \cos \varphi \left[ 1 - \epsilon_3 \cos \varphi \right. \\
 &\quad \left. + \frac{\epsilon_3^2}{2} (3 \cos^2 \varphi - 1) + \frac{\epsilon_3^3}{2} (-5 \cos^3 \varphi + 3 \cos \varphi) \right] d\varphi \\
 &= -\frac{1}{L + R_1 + R_2} (\pi \epsilon_3 + 3\pi \epsilon_3^3 / 8) \\
 &= -\frac{\pi R_2}{(L + R_1 + R_2)^2} - \frac{3\pi R_2^3}{8(L + R_1 + R_2)^4}. \quad (\text{S53})
 \end{aligned}$$

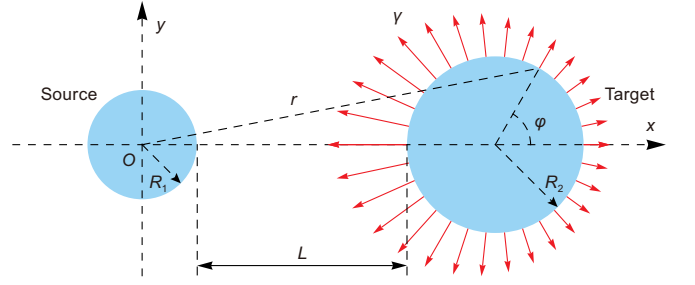


FIG. S8. Attraction between two unequal size binary droplets.

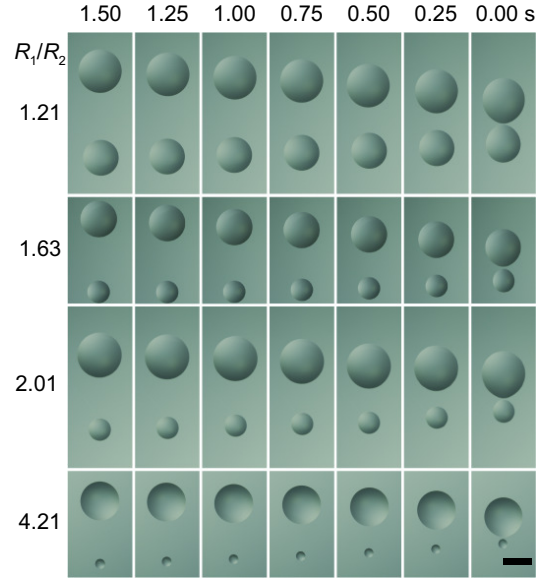


FIG. S9. Top view showing attraction of two 10 wt% PG aqueous sessile droplets with different spreading radius ratio  $\zeta = R_1/R_2$ . The time shown is for  $\tau - t$ . Sequence of images spaced by 0.25 s. The scale bar is 2 mm.

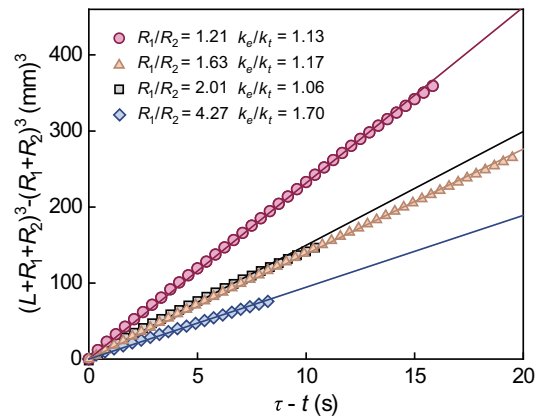


FIG. S10. Data fall into straight lines implying an inverse-square force between 10 wt% PG droplets of different sizes.

Ignoring higher-order terms, the resultant force reads

$$F = -\frac{\gamma_d m_p \phi_\infty \lambda \pi R_1 R_2^2 (1 - \phi_\infty)}{(L + R_1 + R_2)^2}. \quad (\text{S54})$$

The deviation of Eq. S54 from Eq. S53 is  $3\epsilon_3^2/8$ . Denoting the spreading radius ratio of “source” droplet and “target” droplet as  $\zeta = R_1/R_2$ , the definition of  $\epsilon_3$  gives  $\epsilon_3 < 1/(1 + \zeta)$ . From the perspective that the “target” droplet behaves simultaneously as a “source” droplet, we have another spreading radius ratio which is  $1/\zeta$  and the corresponding relationship  $\epsilon_3 < 1/(1 + 1/\zeta)$ . Let us say the interference of high-order terms in Eq. S53 can be ignored if the deviation satisfies

$$\begin{aligned} \frac{3\epsilon_3^2}{8} &< \frac{3}{8} \frac{1}{(1 + \zeta)^2} < 20\% \text{ and} \\ \frac{3\epsilon_3^2}{8} &< \frac{3}{8} \frac{1}{(1 + 1/\zeta)^2} < 20\%. \end{aligned} \quad (\text{S55})$$

Correspondingly, the condition for Eq. S54 to accurately predict the driving force is  $0.37 \leq R_1/R_2 \leq 2.70$ . To verify above analysis, experiments were conducted for droplets with different sizes and part of the results were shown in Fig. S9 and Fig. S10. When radius ratios  $\zeta < 3$ , the calculated  $k_e/k_t$  is nearly equal to 1.

### VIII. INVERSE-SQUARE FORCE BETWEEN FLOATING BINARY DROPLETS ON A LIQUID FREE SURFACE.

Two IPA aqueous droplets partially submersed in an immiscible silicone oil pool will attract each other [10]. Nonuniform vapor density produces a temperature gradient over the cap of the floating droplet and subsequent a thermocapillary stress contributing to droplet motion (Fig. S11, a copy sketch to fig. 4 in Liu & Tran [10]). The evaporation rate per unit area is estimated as

$$\dot{m}_m(\varphi) \sim 1 - \frac{R_c}{r}, \quad (\text{S56})$$

$$r = \sqrt{(L + 2R_s + R_c \cos \varphi)^2 + (R_c \cos \varphi)^2}, \quad (\text{S57})$$

where  $R_c$  is the radius of droplet cap,  $r$  is the distance from the center of “source” droplet, and  $R_s$  is the droplet radius.

The temperature difference  $\Delta T_d(\varphi) \sim [\dot{m}_m(\varphi)]^{1/2}$  across the droplet cap generates a thermocapillary stress  $\tau_d(\varphi) \approx (\gamma_T \Delta T_d(\varphi))/R_c \sim \Delta T_d(\varphi)$ , where  $\gamma_T = \partial\gamma/\partial T$  is derivative of the surface tension  $\gamma$  with respect to  $T$ . Meanwhile, the temperature difference  $\Delta T_o(\varphi) \sim [\dot{m}_m(\varphi)]^{1/2}$  across the surrounding thermally affected area with characteristic distance  $d_a$  generates the stress  $\tau_o(\varphi) \approx (\gamma_T \Delta T_o(\varphi))/d_a \sim \Delta T_d(\varphi)$ . Hence the thermo-

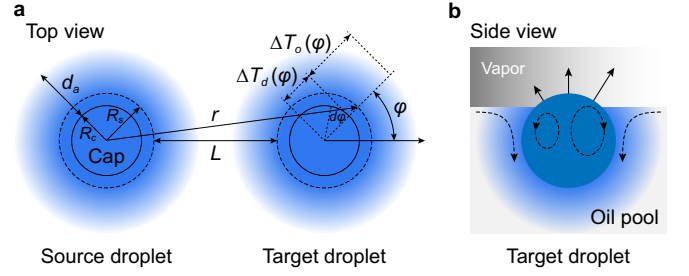


FIG. S11. A schematic diagram showing the geometric parameters and temperature field in the floating droplet system. A copy sketch to fig. 4 in Liu & Tran [10]. (a) Top-view schematic of the system consisting of a “source” and “target” droplet partially immersed into a liquid pool.  $R_s$  and  $R_c$  are droplet radius and cap radius, respectively.  $d_a$  denotes a length scale within which the oil around the droplet will be thermally affected by the lower temperature of the cap. (b) Side-view schematic of the target droplet. Dashed arrows indicate convective flows. Solid arrows indicate nonuniform evaporation across the cap of the target droplet.

capillary stress gradient of droplet cap  $\Gamma_d$  and surrounding thermally affected area  $\Gamma_o$  are

$$\begin{aligned} \Gamma_d &= \frac{d\tau_d}{dr} \sim \frac{d}{dr} \left(1 - \frac{R_c}{r}\right)^{1/2} \sim \frac{1}{(1 - R_c/r)^{1/2}} \frac{1}{r^2}, \\ \Gamma_o &= \frac{d\tau_o}{dr} \sim \frac{d}{dr} \left(1 - \frac{R_c}{r}\right)^{1/2} \sim \frac{1}{(1 - R_c/r)^{1/2}} \frac{1}{r^2}, \end{aligned} \quad (\text{S58})$$

respectively. When the distance  $r \gg R_c$ , the thermocapillary stress of droplet cap and surrounding thermally affected area can be expressed as

$$\begin{aligned} F_d &\sim \Gamma_d R \cdot \pi R^2 \sim \Gamma_d \sim \frac{1}{r^2}, \\ F_o &\sim \Gamma_o R \cdot \pi R^2 \sim \Gamma_o \sim \frac{1}{r^2}. \end{aligned} \quad (\text{S59})$$

The resultant thermocapillary stress is

$$F = F_d + F_o \sim \frac{1}{r^2}. \quad (\text{S60})$$

Eventually, we obtain an inverse-square attractive force between floating binary droplets on a liquid free surface. The viscous drag is  $F_d \sim U$  and the kinematic relationship for droplet motion can be described as

$$(L_0 + 2R)^3 - (L + 2R)^3 \sim t, \quad (\text{S61})$$

where  $L_0$  is the initial distance between droplets. Experimental verification of Eq. S61 is shown in Fig. 4d in the main text. When the distance between droplets is smaller than a critical distance, the thermally affected regions of the droplet couples overlap and brings other force into play and interferes droplet motion.

### IX. COMPARISON WITH THE LAW OF UNIVERSAL GRAVITATION.

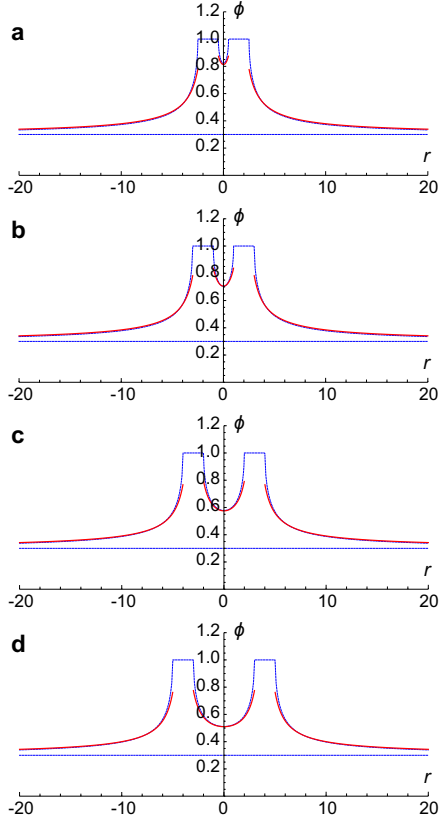


FIG. S12. Verification for superposition principle. (a), (b), (c) and (d) compares the numerical results (blue dash lines) with theoretical results (red solid lines), for total humidity distribution from two “source” droplets  $L = R, 2R, 4R$  and  $6R$  apart, respectively.

The gravitational potential of a “source” with mass  $M$ , and the gravitation of a “target” with mass  $m$  in the gravitational field of above “source” are

$$E = \int_{\infty}^r \frac{GM}{r^2} dr = -\left. \frac{GM}{r} \right|_{\infty} = -\frac{GM}{r},$$

$$F_m = \frac{GMm}{r^2}, \quad (\text{S62})$$

respectively, where  $G$  is the gravitational constant. The gravitation can be written as mass multiplied by the gradient of the gravitational potential  $F_m = -m\nabla E$ . Here, we define a humidity potential induced by evaporation  $E' = -G'M'/r = -\gamma_d m_p \phi_{\infty} \lambda'(1 - \phi_{\infty}) R_1 / r$ , where  $G' = d\gamma/d\phi = \gamma_d m_p \phi_{\infty}$  is a constant denoting the derivative of surface tension to environment humidity,  $M' = \lambda'(1 - \phi_{\infty}) R_1$  represents the decay coefficient of humidity away from the “source” droplet,  $m' = \pi R_2^2$  represents the wetting area of the “target” droplet, respectively. In an identical coordinate system as the universal gravitation, the resultant force exerted on the “target”

droplet in the humidity field of the “source” droplet reads

$$F = \pi R_2^2 \Gamma = \pi R_2^2 \nabla \gamma = \pi R_2^2 \frac{d\gamma}{d\phi} \nabla \phi$$

$$= \gamma_d m_p \phi_{\infty} \pi R_2^2 \frac{\lambda'(1 - \phi_{\infty}) R_1}{r^2}. \quad (\text{S63})$$

Next we investigate whether  $F$  satisfies the superposition principle. For an ideal small “target” object with mass  $m$  in the vicinity of two “source” objects with mass  $M$ , and assume the existence of  $m$  does not affect the gravitational potential fields of the “source” objects, the resultant gravitational potential and gravitation read

$$E = \int_{\infty}^{\vec{r}} \left( \frac{GM}{r_1^2} \vec{n}_1 + \frac{GM}{r_2^2} \vec{n}_2 \right) \cdot d\vec{r}$$

$$= -\frac{GM}{r_1} - \frac{GM}{r_2}, \quad (\text{S64})$$

$$F_m = \frac{GMm}{r_1^2} \vec{n}_1 + \frac{GMm}{r_2^2} \vec{n}_2, \quad (\text{S65})$$

respectively, where  $r_1$  and  $r_2$  are distances between “target” and the two “source” objects,  $\vec{n}_1$  and  $\vec{n}_2$  are the unit vectors pointing from center of “target” to the center of two “source” objects, respectively.

The superposition of the humidity field is not that straightforward as there is an upper limit for humidity, which is 1. We invoke a coefficient  $\lambda'$  to guarantee the validity of humidity range. Figure S12 shows the numerical results of the humidity distribution on the central axis of two “source” droplets with different spacing, verifying the feasibility of describing humidity distribution as

$$\phi = \frac{\lambda'(1 - \phi_{\infty}) R}{r_1} + \frac{\lambda'(1 - \phi_{\infty}) R}{r_2} + \phi_{\infty}, \quad (\text{S66})$$

where  $\lambda' = 0.55, 0.58, 0.59, 0.60$  for  $L = R, 2R, 4R$  and  $6R$ , respectively. Analogously, the resultant force exerted on a “target” droplet with spreading radius  $a$  in the humidity field of two “source” droplets with spreading radius  $R$  can be expressed in a similar form to the law of universal gravitation (Fig. 5 in the main text)

$$F = \pi a^2 \Gamma = \pi a^2 \nabla \gamma = \pi a^2 \frac{d\gamma}{d\phi} \nabla \phi$$

$$= \pi a^2 \frac{d\gamma}{d\phi} \nabla (\phi_1 + \phi_2)$$

$$= \gamma_d m_p \phi_{\infty} \pi a^2 \frac{\lambda'(1 - \phi_{\infty}) R}{r_1^2} \vec{n}_1$$

$$+ \gamma_d m_p \phi_{\infty} \pi a^2 \frac{\lambda'(1 - \phi_{\infty}) R}{r_2^2} \vec{n}_2$$

$$= \frac{G'M'm'}{r_1^2} \vec{n}_1 + \frac{G'M'm'}{r_2^2} \vec{n}_2, \quad (\text{S67})$$

where  $G' = \gamma_d m_p \phi_{\infty}$ ,  $M' = \lambda'(1 - \phi_{\infty}) R$ ,  $m' = \pi a^2$ ,  $\vec{n}_1$  and  $\vec{n}_2$  are the unit vectors pointing from center of “target” to the center of two “source” droplets, respectively. Clearly, Eq. S67 indicates that the driving force in this study satisfies the superposition principle.

- 
- [1] H. Hu and R. G. Larson, Evaporation of a sessile droplet on a substrate, *The Journal of Physical Chemistry B* **106**, 1334 (2002).
- [2] N. J. Cira, A. Benusiglio, and M. Prakash, Vapour-mediated sensing and motility in two-component droplets, *Nature* **519**, 446-450 (2015).
- [3] S. Karpitschka, F. Liebig, and H. Riegler, Marangoni contraction of evaporating sessile droplets of binary mixtures, *Langmuir* **33**, 4682-4687 (2017).
- [4] J. Bico and D. Quéré, Falling Slugs, *Journal of Colloid and Interface Science* **243**, 262 (2001).
- [5] F. Brochard, Motions of droplets on solid surfaces induced by chemical or thermal gradients, *Langmuir* **5**, 432-438 (1989).
- [6] E. Rio, A. Daerr, B. Andreotti, and L. Limat, Boundary conditions in the vicinity of a dynamic contact line: Experimental investigation of viscous drops sliding down an inclined plane, *Physical Review Letters* **94**, 024503 (2005).
- [7] C. Huh and L. Scriven, Hydrodynamic model of steady movement of a solid/liquid/fluid contact line, *Journal of Colloid and Interface Science* **35**, 85 (1971).
- [8] R. L. Hoffman, A study of the advancing interface. I. Interface shape in liquid—gas systems, *Journal of Colloid and Interface Science* **50**, 228 (1975).
- [9] E. Reyssat, Drops and bubbles in wedges, *Journal of Fluid Mechanics* **748**, 641-662 (2014).
- [10] D. Liu and T. Tran, Vapor-induced attraction of floating droplets, *The Journal of Physical Chemistry Letters* **9**, 4771-4775 (2018).